Targeted Cyclo[8]pyrrole-based NIR-II Photoacoustic Tomography Probe for Suppression of Orthotopic Pancreatic Tumor Growth and Intra-abdominal Metastases

Jingqin Chen[1,8,*], Rui Chen[1,2,6,7,8], Calvin V. Chau[3,8], Adam C. Sedgwick[4,8], Qiang Xue[1], Tao Chen[1], Silue Zeng[1,2], Ningbo Chen[1,5], Kenneth K. Y. Wong[5], Liang Song[1], Yaguang Ren[1,*], Jian Yang[2,6,*], Jonathan L. Sessler[3,*], and Chengbo Liu[1,*]

[1] *Research Center for Biomedical Optics and Molecular Imaging, Key Laboratory of Biomedical Imaging Science and Systems, Shenzhen Institute of Advanced Technology, Chinese Academy of Sciences, Shenzhen 518055, China*

[2] *Department of Hepatobiliary Surgery I, General Surgery Center, Zhujiang Hospital, Southern Medical University, Guangzhou 510280, China*

[3] *Department of Chemistry, University of Texas at Austin, 105 East 24th Street A5300, Austin, Texas 78712-1224, United States*

[4] *Department of Chemistry, Kings College London, 7 Trinity Street, London, SE1 1DB, U.K.*

[5] *The University of Hong Kong, Department of Electrical and Electronic Engineering, Hong Kong, China*

[6] *Guangdong Provincial Clinical and Engineering Center of Digital Medicine, Guangzhou 510280, China*

[7] *Biliary Surgical Department of West China Hospital, Sichuan University, Chengdu 610064, China*

[8] *Equal contribution*

ABSTRACT: Pancreatic cancer is highly lethal. New diagnostic and treatment modalities are desperately needed. We report here that an expanded porphyrin, cyclo[8]pyrrole (CP), with a high extinction coefficient (89.16 L/g•cm) within the second near-infrared window (NIR-II) may be formulated with an $\alpha_v\beta_3$ specific targeting peptide, cyclic-Arg-Gly-Asp (cRGD), to form cRGD-CP nanoparticles (cRGD-CPNPs) with promising NIR-II photothermal (PT) therapeutic and photoacoustic (PA) imaging properties. Studies with a ring-array PA tomography system, coupled with analysis of control nanoparticles lacking a targeting element (CPNPs), revealed that cRGD conjugation promoted the delivery of the NPs through abnormal vessels around the tumor to the solid tumor core. This proved true in both subcutaneous and orthotopic pancreatic tumor mice models, as confirmed by immunofluorescent studies. In combination with NIR-II laser photoirradiation, the cRGD-CPNPs provided near-baseline tumor growth inhibition through PTT both in vitro and in vivo. Notably, the combination of the present cRGD-CPNPs and photoirradiation was found to inhibit intra-abdominal metastases in an orthotopic pancreatic tumor mouse model. The cRGD-CPNPs also displayed good biosafety profiles as inferred from PA tomography, blood analyses, and H&E staining. They thus appear promising for use in combined PA imaging and PT therapeutic treatment of pancreatic cancer.

INTRODUCTION

The 5-year survival rate for pancreatic cancer is approximately 10%, a rate that seen little improvement during the past 40 years.[1-3] Most patients with pancreatic cancer remain asymptomatic until the disease reaches an advanced stage, reflecting a lack of clear symptoms and diagnostic limitations that allows the disease to elude detection during its formative stages.[4-5] Traditional medical imaging techniques, such as X-ray computed tomography (CT), magnetic resonance imaging (MRI), and ultrasound (US), are rarely able to detect pancreatic cancer in its early stage (lesions ≤1 cm in size).[6-8] On the other hand, molecular-based imaging can be effective in detecting molecular and physiological alterations that occur before tumor anatomic changes.[9] For example, fluorine-18-fluorodeoxy-*D*-glucose positron emission tomography (FDG-PET) can allow the early detection of pancreatic cancer, although the use of radioisotopes is a concern.[10-11]

Photoacoustic (PA) molecular imaging is a relatively new imaging modality.[12] It combines the advantage of both PA imaging (PAI) and the specificity of molecular probes.[13-16] PAI operates on the principle of "light in and sound out" and thus benefits from the use of exogenous probes that absorb externally light and produce local

heating. In addition to producing photoacoustic waves, this local heating can trigger a photothermal therapeutic (PTT) effect.[17-20] To date, a variety of exogenous PA probes, including inorganic and carbon-based materials, organic semiconducting conjugated polymers, and porphyrins have been explored in the context of PAI and PTT.[18, 21-25] So-called expanded porphyrins appear particularly attractive in this regard since they often possess absorption features that are shifted into the second near-infrared window (NIR-II)[26-29] where tissues are more transparent.[30-33] Here we report a set of nanoparticles (NPs), referred to as cRGD-CPNPs, that show promise for the PA-based imaging and PT-induced treatment of pancreatic cancer as inferred from in vivo murine model studies.

The cRGD-CPNPs of the present study comprise an expanded porphyrin, cyclo[8]pyrrole (CP), that absorbs in the NIR-II spectral region combined with an integrin $\alpha_v\beta_3$ receptor ligand, cyclic-Arg-Gly-Asp (cRGD). Integrin $\alpha_v\beta_3$ receptors are transmembrane glycoproteins that are highly expressed by not only by the endothelial cells of new tumor vessels, but also by pancreatic cancer cells.[34-35] They are thus promising tumor markers for drug delivery.[36] As detailed below, the targeting of cRGD-CPNPs to pancreatic tumors in both subcutaneous and orthotopic pancreatic tumor mice models was confirmed using a ring-array PA tomography system (Scheme 1). Moreover, guided by the resulting PA images, the pancreatic tumors in subcutaneous and orthotopic mouse models could be irradiated by a NIR-II laser and effectively suppressed. Meanwhile, the development of abdominal metastases was inhibited compared to control group. Support for an acceptable biosafety profile came from a combination of PA tomography, blood analyses, and H&E staining.

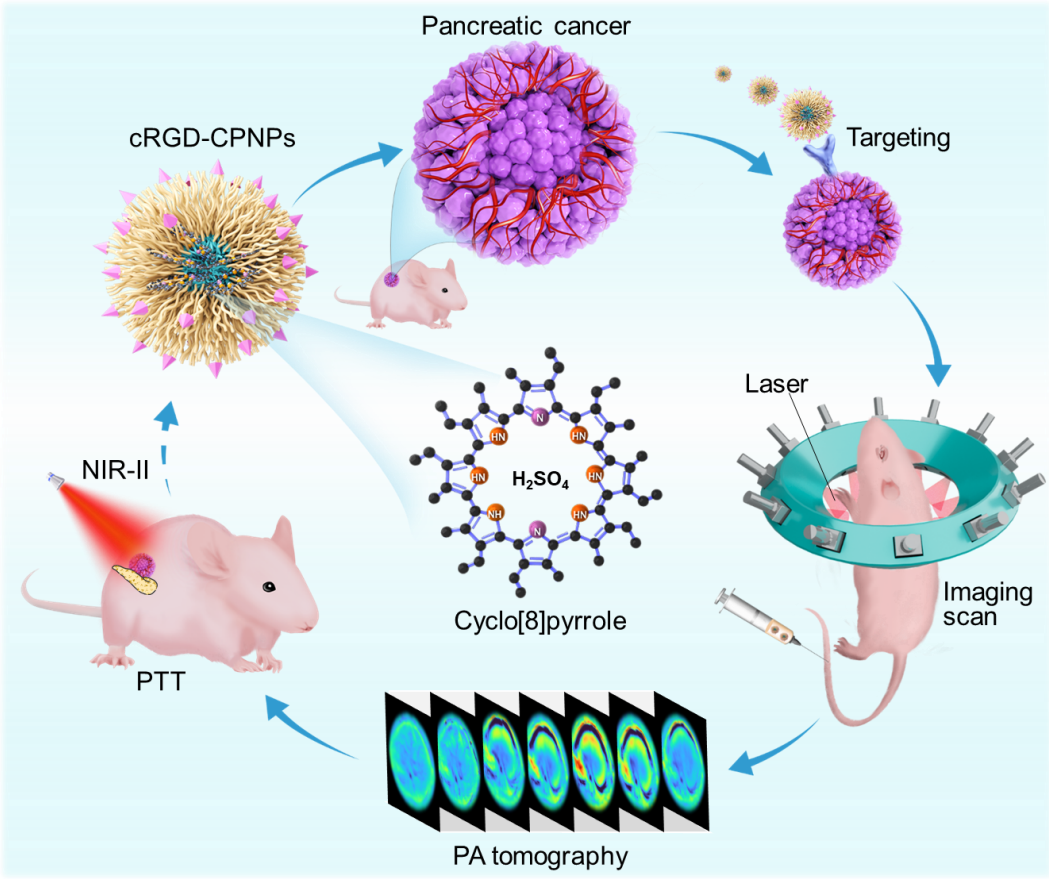

Scheme 1. Schematic view of the proposed targeting of cyclo[8]pyrrole-cRGD nanoparticles (cRGD-CPNPs) to orthotopic pancreatic cancer in murine model. Also shown is the photoacoustic (PA) tomography imaging and photothermal therapy (PTT) the cRGD-CPNPs probes are expected to allow. NIR-II: second near-infrared region.

RESULTS AND DISCUSSION

Preparation and Characterization of cRGD-CPNPs. The octapyrrolic porphyrinoid (CP) used in this study was chosen because it displays a strong absorbance (extinction coefficient = 89.16 L/g•cm) in the NIR-II region (λ_{max} = 1064 nm; Figure S1). To enhance the water solubility of CP for potential use in PAI and PTT applications, CP was encapsulated within a functionalized surfactant (1,2-distearoyl-sn-glycero-3-phosphoethanolamine-polyethylene glycol (DSPE-PEG_{2000}) conjugated to cRGD (DSPE-PEG_{2000}-cRGD)) via nanoprecipitation (Figure 1A) to give cRGD-CPNPs. As a control, CPs encapsulated with DSPE-PEG_{2000}

without cRGD (CPNPs) were also prepared via the same method.

As shown in Figure 1B, the ratio between DSPE-PEG_{2000} and CP affects the CP-derived absorbance at 1064 nm. Presumably, this reflects the fact that different relative concentrations of DSPE-PEG_{2000} influence the extent of aggregation within the nanoparticle. Increasing the ratio of DSPE-PEG_{2000} and CP from 10:1 to 20:1 led to an enhancement in the absorbance and extinction coefficient at 1064 nm, as well as the diameter (Table S1). The results provide support for the above hypothesis, namely that increasing concentration of DSPE-PEG2000 serves to increase the size of the NPs, while enhancing the dispersibility of the CP in the NPs. However, high ratios of DSPE-PEG_{2000} were found to increase the cytotoxicity of the NPs (Figure 1C). In light of this, a 15:1 DSPE-PEG_{2000}:CP ratio was used in all subsequent nanoparticle formulations. Transmission electron microscopy (TEM) revealed that the cRGD-CPNPs obtained at this ratio were spherical with a core-shell structure (Figure S2A). An average diameter of 98.5 nm was determined via dynamic light scattering (DLS) (Figure S2B). The cRGD-CPNPs showed no obvious change in diameter after being stored for 7 days at room temperature in phosphate-buffered saline (PBS; pH 7.4; Figure S3). The cRGD-CPNPs prepared in this way, displayed an absorption band in the NIR-II region centered around 1064 nm (Figure 1D and Table S1) with an extinction coefficient of 49.7 L/g•cm.[30, 37-38] The photothermal conversion efficiency was found to be 41.3% (Figure 1E). This value is competitive with the most promising NIR-II organic photothermal reagents reported to date.[39-40] In addition, cRGD was conjugated with PEG via a covalent bond to produce cRGD-CPNPs. We tested the stability of the resulting construct in the presence of glutathione (GSH) by monitoring the change in the characteristic cRGD absorbance feature around 210 nm upon incubation with different concentrations of GSH for 3 h at 37 °C. A minimal change was seen (Fig. S4). These results are taken as evidence that the cRGD-CPNPs are stable in the presence of GSH under physiological conditions for the timescale of the present study.

To test whether integrin $\alpha_v\beta_3$-based tumor targeting was seen for the cRGD-CPNPs, fluorescein isothiocyanate (FITC) was used to label the NPs (Figure S5). An increased FITC fluorescence signal was seen for cRGD-CPNPs-treated Panc02 pancreatic cancer cells compared to those treated with just CPNPs (cf. Figure 1F and Figure S6). This difference is ascribed to the pancreatic cell selectivity and high binding affinity displayed by the cRGD motif for the Panc02 integrin $\alpha_v\beta_3$ cell receptors.[41-42] To test further the presumed specificity of cRGD in pancreatic cancer targeting, differences in cRGD receptor integrin $\alpha_v\beta_3$ expression between pancreatic cancer tissue and paracancerous tissue from 179 patients were analyzed using publicly available data sources and standard bioinformatics methods, namely a gene expression profiling interactive analysis (GEPIA).[43-45] The results obtained from this screen confirmed that integrin $\alpha_v\beta_3$ was overexpressed in pancreatic cancer in contrast to paracancerous tissue (Figure 1G). This data analysis also revealed that the 5-year survival probability for patients with high cRGD receptor expression was worse than for patients with low cRGD receptor levels (Figure 1H). To the extent this conclusion is correct, it provides support for the notion that integrin $\alpha_v\beta_3$ constitutes an attractive therapeutic target for pancreatic cancer drug design.[35, 46]

PA Properties of cRGD-CPNPs. To determine the NIR-II PA properties of cRGD-CPNPs, a custom-built PA imaging system was used.[47-48] In water (pH =7.4), a linear correlation between PA intensity and cRGD-CPNPs concentration was seen (Figure 2A and B). Effective visualization was still apparent at cRGD-CPNPs concentrations as low as ca. 20 μg/mL under 1064 nm pulsed laser photoirradiation at a fluence rate of ca. 6 mJ/cm^2. The photothermal effect and PA signal of cRGD-CPNPs with different DSPE-PEG_{2000} and CP ratios was also investigated. As shown in Table S2, with an increase in the ratio, the photothermal effect and PA signal of cRGD-CPNPs likewise increased. On the other hand, we note that CP dissolved in the non-biocompatible solvent DCM showed the highest photothermal effect and PA signal.

No obvious changes in the PA signal were observed even after subjecting to 1000 laser pulses at 1064 nm (Figure 2C). The cRGD-CPNPs displayed better long-term photostability than indocyanine green (ICG), an FDA approved agent used as a positive control (Figure 2D). For instance, in the case of ICG a statistically significant decrease in the absorption intensity was seen after 7 days under natural light, whereas no discernible change was seen for the cRGD-CPNPs under otherwise identical conditions. Differences in the solution color were seen for ICG, but not for the cRGD-CPNPs (Figure S7).

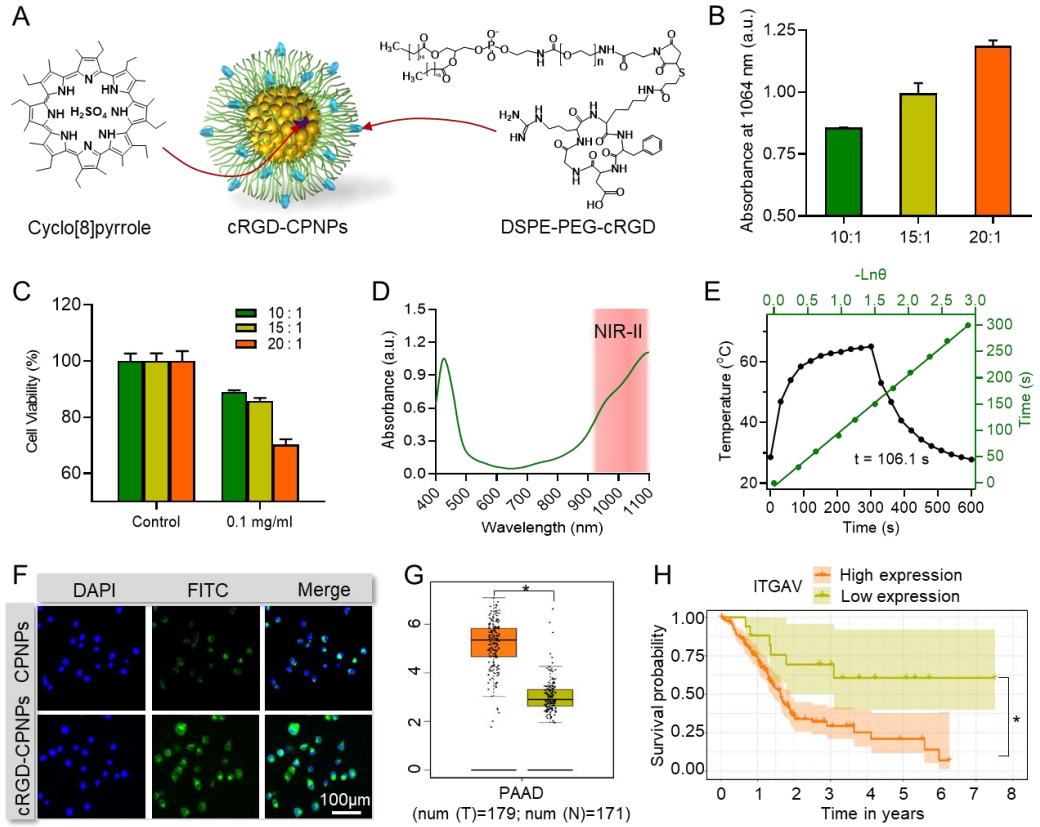

Figure 1. Preparation and characterization of cRGD-CPNPs. (A) Preparation of cRGD-CPNPs from cyclo[8]pyrrole. (B) Absorbance at 1064 nm for mixtures containing different ratios of DSPE-PEG_{2000} and cyclo[8]pyrrole. (C) Cytotoxicity study of the mixtures used in (B). (D) Absorbance spectrum of cRGD-CPNPs (prepared using a 15:1 DSPE-PEG_{2000}:CP ratio) in water. (E) Calculation of the photothermal conversion efficiency and the warming and cooling seen when aqueous solutions of cRGD-CPNPs are subject to on-off photo-irradiation at 1 W/cm^2. (F) Fluorescence images of cells incubated with CPNPs and cRGD-CPNPs (labelled with FITC). (G) Gene expression levels of integrin subunit alpha-V gene (ITGAV) in pancreatic cancer tumor and matching normal tissues. (H) Kaplan-Meier analysis of ITGAV in TCGA-PAAD. GEPIA: gene expression profiling interactive analysis; TCGA: the cancer genome atlas; PAAD: pancreatic adenocarcinoma. * p <0.05.

To assess whether cRGD-CPNPs would provide NIR-II sensitivity in biological tissues, several tubes containing cRGD-CPNPs (0.5 mg/mL solutions) were embedded at varying depth levels in chicken breast slices and imaged from the top (Figure 2E). The B-scan (vertical section) PA images revealed a discernible cRGD-CPNPs-induced PA signal at depths as great as 2 cm under 1064 nm pulsed laser irradiation (Figure 2F and G). Next, samples of cRGD-CPNPs (100 μL, 0.2 mg/mL) mixed with matrigel (v:v = 1:1) were injected subcutaneously into the back of a BALB/c nude mouse. PA images were then captured under 808 nm and 1064 nm laser irradiation (Figure 2H). The PA image at 1064 nm displayed a signal-to-noise ratio (SNR) as high as 24.4 dB, approximately 2-fold higher than at 808 nm (Figure 2I). A ca. 2x enhancement in the PA signal (relative to pre-injection) was also seen when the cRGD-CPNPs (mixed with matrigel; v:v = 1:1) were injected into the pancreatic region and imaged under 1064 nm laser irradiation (Figure 2J, K, and Figure S8). The improvement seen on moving from 808 to 1064 nm is ascribed to the strong 1064 nm absorbance of the cRGD-CPNPs, reduced light scattering in the NIR-II region, and lower laser energy attenuation through biological tissues at longer wavelengths.[49] As expected based on the principles of photothermal effects and PA imaging, the stronger the laser intensity, the higher the laser fluence per unit area of NPs, and the better the PA signal and photothermal effect. Also, the higher the concentration of the NPs, the greater the absorbance, and the more intense the PA signal and photothermal effect.

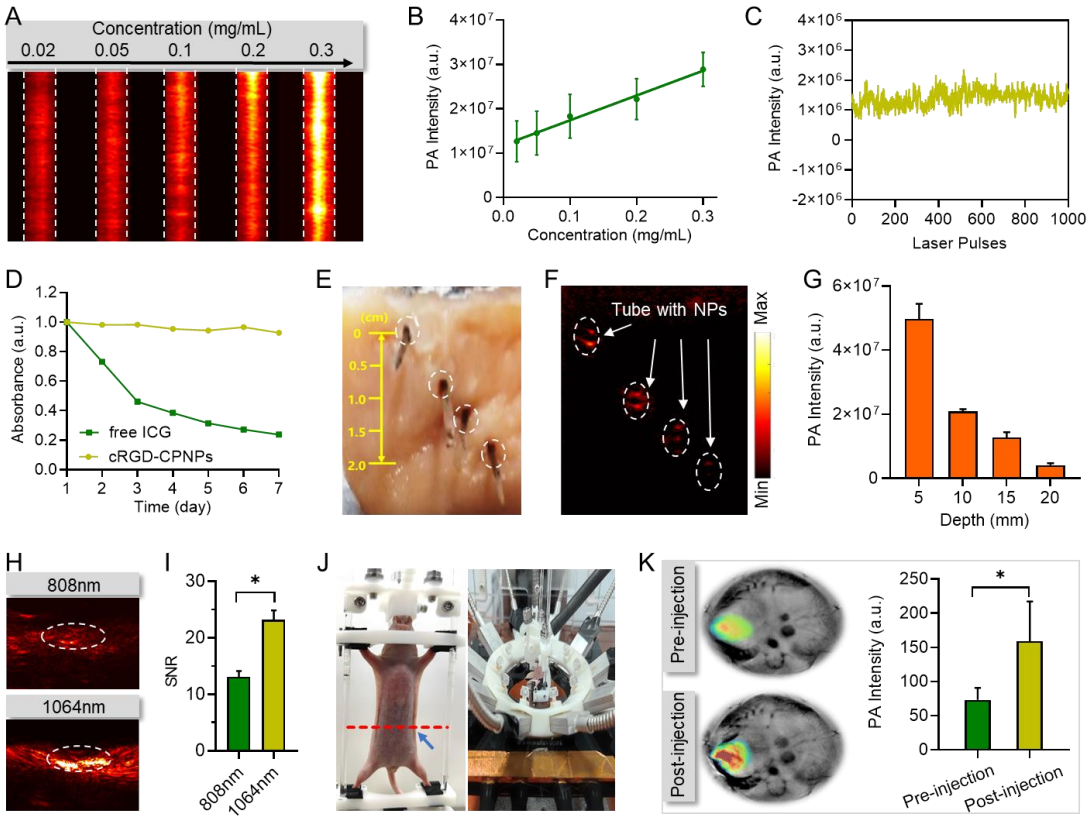

Figure 2. PA properties of cRGD-CPNPs. (A and B) PA images (A) and intensity (B) of cRGD-CPNPs at different concentrations (0.02, 0.05, 0.1, 0.2 and 0.3 mg/mL) in water. (C) PA signal intensity of cRGD-CPNPs after exposure to 1000 laser pulses. (D) Change in absorbance at 1064 nm of cRGD-CPNPs and free ICG seen over the course of 7 days. (E) Tubes containing cRGD-CPNPs inserted into chicken breast for phantom PA experiments. PA images (F) and intensity (G) of cRGD-CPNPs tubes at varying depth levels in chicken breast. PA images (H) and signal-to-noise ratio (I) of cRGD-CPNPs injected subcutaneously to a mouse back monitored at 808 nm or 1064 nm. **p* <0.05. (J) Photo of a mouse constrained in the imaging setup used in the present study. The blue arrow indicates the pancreatic region where the cRGD-CPNPs were injected; the red dotted line indicates the imaging section. (K) PA images and intensity of the mouse pancreas before and after injecting cRGD-CPNPs and subjecting to 1064 nm pulsed laser photoirradiation. **p* <0.05.

In Vivo NIR-II PAI. A custom made NIR-II ring-array PA tomography system in conjunction with a subcutaneous pancreatic tumor BALB/c nude mouse model was used to assess the in vivo targeting of cRGD-CPNPs. After the tumor grew to ~80 mm^3, the mice were evenly divided into two groups of 3 mice each, namely mice injected with CPNPs and mice injected with cRGD-CPNPs (the same concentration of CP was used in both groups). Based on the results shown in Figures 3A and B, both groups displayed a similar PA intensity distribution over the span of 24 h. Whereas a low PA signal was seen pre-injection, analysis 5 min post-injection revealed both groups peaking. This enhancement was ascribed to the presence of these two probes in the epidermal blood. The PA signal then decreased, before peaking a second time at ca. 9 h post-injection. The PA signals in the CPNPs injected group were mainly distributed around the tumor. In contrast, the PA signals in the cRGD-CPNPs injected group were distributed throughout the tumor (Figure 3C). This difference in localization is interpreted in terms of the cRGD-CPNPs being internalized well, but the unfunctionalized CPNPs, in contrast, being unable to enter the tumor core.

Solid tumors have been reported to contain abnormal blood vessels mainly distributed around the tumor tissue.[50-51] This heterogeneity is generally viewed as being unfavorable for the delivery of probes and therapeutic agents (Figure 3D). In Figure 3E, the CD31-labeled blood vessels can be clearly seen surrounding the pancreatic tumor. Moreover, CD61/CD51-labeled integrin $\alpha_v\beta_3$ were observed, not only in blood vessel endothelial cells, but also in pancreatic cancer cells, providing a target site for the cRGD-CPNPs to bind. On this basis, we expect that the cRGD moieties present in the cRGD-CPNPs will serve not only to enhance their targeting to pancreatic tumors sites but also their distribution throughout the cancerous lesion.

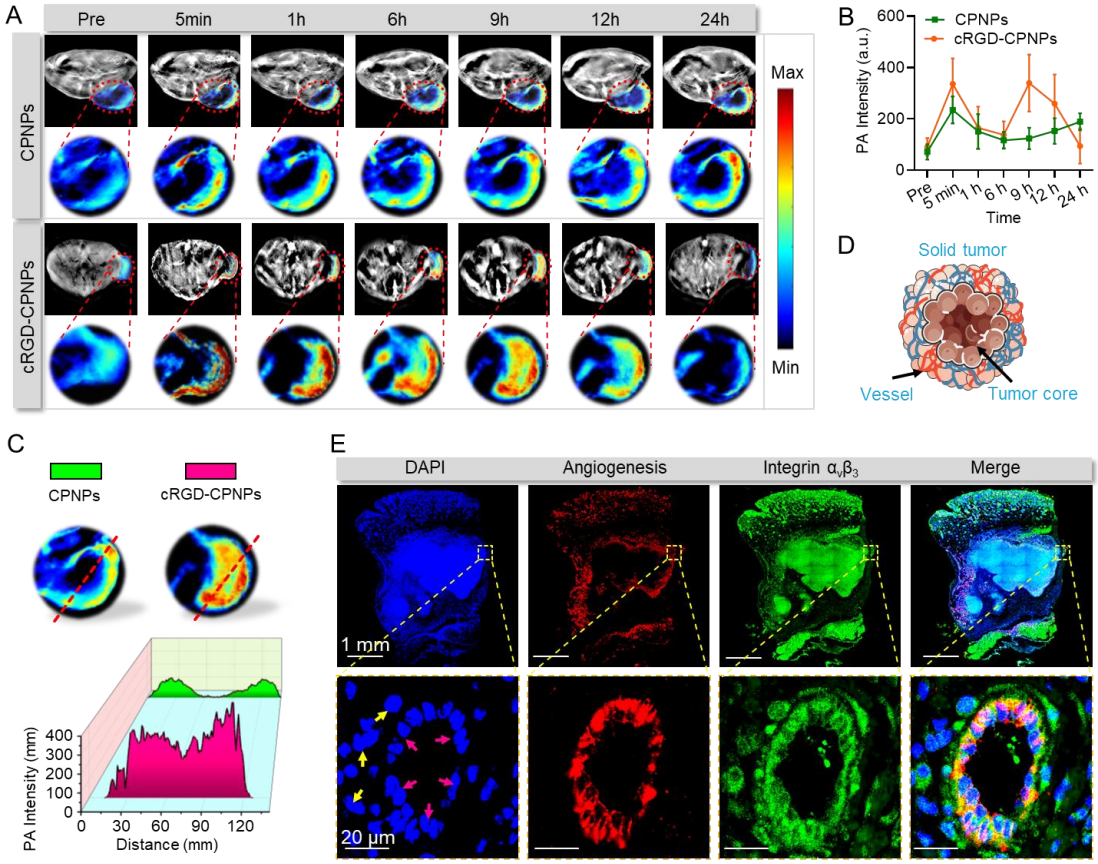

Figure 3. In vivo PA tomography of a subcutaneous pancreatic tumor mouse model. (A) In vivo PA tomography of subcutaneous pancreatic tumor-bearing mice before and after injection with CPNPs and cRGD-CPNPs. (B) Quantitative PA signal of the tumor groups subject to injection with CPNPs and cRGD-CPNPs. (C) PA intensity cross-section of the CPNPs and cRGD-CPNPs injected tumor groups. (D) Schematic view of the solid tumor cross-section. (E) Cross-sectional immunofluorescence images of a solid tumor. Cell nuclei were stained with DAPI (blue), blood vessels were stained with CD31 (red), while integrin $\alpha_v\beta_3$ was stained with CD61 + CD51 (green). Yellow arrows indicate tumor cells and pink arrows indicate vessel walls.

The in vivo tumor targeting of the cRGD-CPNPs was also evaluated using a Panc02 orthotopic pancreatic tumor BALB/c nude mouse model, which was built using a modification of a method described in a previous report.[52] For this model, matrigel was mixed with Panc02 cells before injecting the resulting formulation into the pancreatic parenchyma in situ so as to prevent peritoneal leakage of the cells. After tumor establishment, the mice were injected intravenously with either CPNPs or cRGD-CPNPs. Bioluminescence analyses confirmed the presence of the pancreatic tumor growing beside the spleen (Figure 4A). After tail vein injection of the NPs, PA imaging revealed an increased PA signal in the spleen, likely as the result of lymphatic drainage. These signals remained at a high level for 24 h in both the CPNPs and cRGD-CPNPs groups (Figure 4B and D). The CPNPs and cRGD-CPNPs groups also displayed persistent PA signals in the tumor region. At 9 h post-injection, the PA signal of the tumor in the cRGD-CPNPs group was significantly higher than that in the CPNPs group (Figure 4B and C), likely due to the cRGD conjugation onto the CPNPs which acts to enhance accumulation of the NPs in the tumor. Excision of both the pancreatic tumor and spleen confirmed that the PA signal ascribed to the tumor, was not due to overlap with the spleen (Figure 4D and E). Hematoxylin-eosin (HE) staining of the tumor mass reconfirmed that the mass observed was a tumor (Figure 4F). Overall, these results provide support for the design expectation that cRGD-CPNPs in conjuncture with NIR-II ring-array PA tomography can be used to locate and image orthotopic pancreatic tumors.

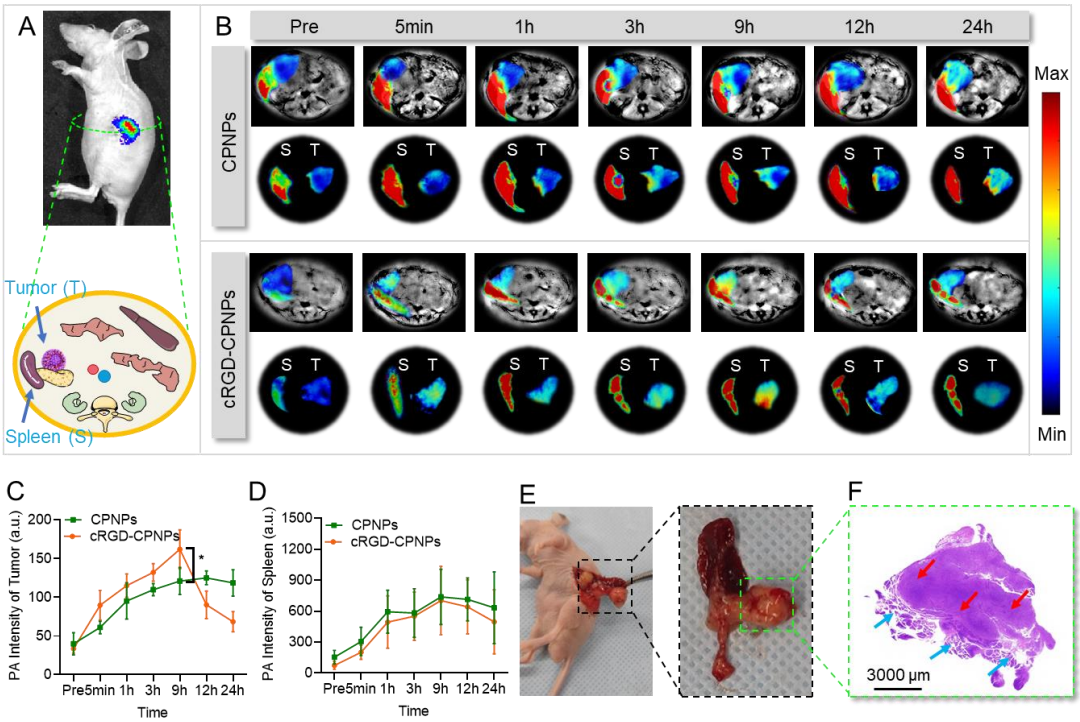

Figure 4. In vivo PA tomography of orthotopic pancreatic tumor. (A) In vivo bioluminescence image of an orthotopic pancreatic tumor mouse model. Inset is the cross-sectional scheme of the mouse. (B) In vivo PA tomography of orthotopic pancreatic tumor-bearing mice before and after injection with CPNPs and cRGD-CPNPs. S: spleen, T: tumor. (C and D) Quantitative PA signal of the tumor (C) and the spleen (D); *p <0.05. (E and F) Photograph (E) and hematoxylin-eosin (HE) image (F) of the excised orthotopic pancreatic tumor. Red arrows indicate tumor cells and blue arrows indicate pancreatic cells.

In Vitro and In Vivo PTT. Given the tumor localization inferred from the above studies, we sought to test whether the cRGD-CPNPs could be used for PTT. With this objective in mind, the photothermal capabilities of the cRGD-CPNPs were assessed.[39, 53] The PTT setup used in this work is shown in Figure S9. The temperature of a 20 μg/mL cRGD-CPNPs solution in water at pH 7.4 was found to reach 86.2 °C after subjecting to photoirradiation for 5 min (1064 nm laser; 1 W/cm^2, Figure S10-S11). After five cycles of "on/off" laser irradiation, the cRGD-CPNPs solution maintained its high photothermal performance. In contrast, a significant decrease in photothermal efficiency was seen for analogous ICG solutions. This difference in photostability was reflected in the colors of the respective samples (Figure S12).

The in vivo PTT utility of the cRGD-CPNPs was assessed per the timeline shown in Figure 5A. As a prelude to these studies, the viability of Panc02 cells treated with cRGD-CPNPs and subject to 1064 nm laser irradiation (5 min, 1 W/cm^2) was assessed. As shown in Figure 5B, a ca. 80%, reduction in cell viability was seen in the presence of 100 μg/mL cRGD-CPNPs. This in vitro PTT effect was roughly 2x greater than what was seen with the CPNPs under identical study conditions. Cell killing was confirmed by a live/dead dual-staining (Figure 5C).

For tests of in vivo PTT efficacy, 25 subcutaneous pancreatic tumor-bearing mice were divided into 5 groups (n = 5/group). These groups were used to study the effect of injection with PBS and cRGD-CPNPs in the absence and presence of photo-irradiation. A group consisting of CPNPs + laser was included. Nine hours post-injection, in the appropriate groups, the tumors were subjected to 1064 nm laser irradiation (5 min, 1 W/cm^2). As can be seen in Figure 5D, the tumor temperature in the cRGD-CPNPs + laser group increased to 55 °C. This value is higher than what was seen in the other groups, including the CPNPs + laser group (Figure S13). No evidence of tumor growth was seen in the cRGD-CPNPs + laser group (3 injections followed by laser irradiation) 18 days post-initial injection (study endpoint). In contrast, the other treatment groups showed tumor growth that mirrored that seen for the PBS control group. Following study termination, the tumors were excised and the relative tumor volumes, morphologies, and staining histologies assessed (Figure 5E-H). Little weight loss was seen throughout the course of treatment for any of the groups (Figure 5I). This was taken as an initial indication that cRGD-CPNPs + laser treatment might prove sufficiently safe for use in PTT.

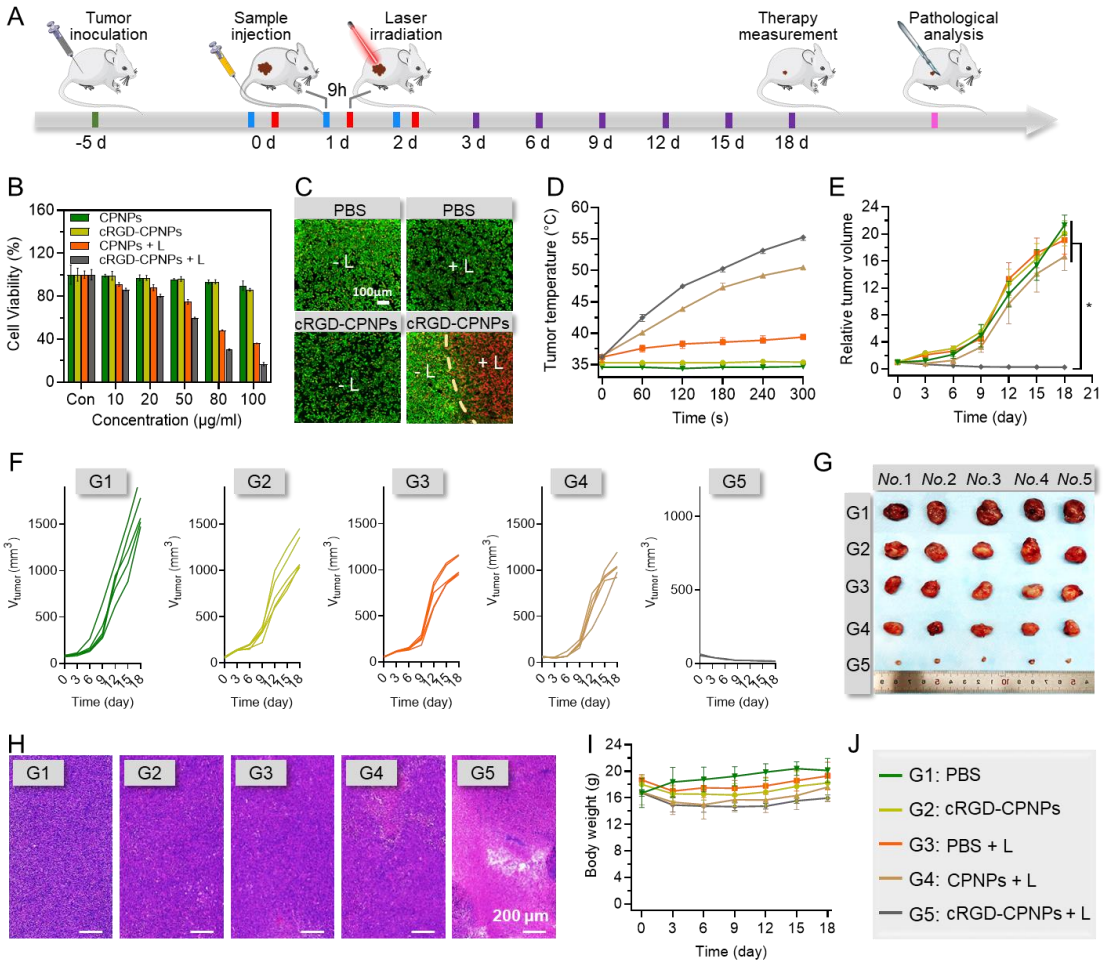

Figure 5. In vitro and in vivo PA guided PTT in a subcutaneous pancreatic tumor model. (A) In vivo PTT of subcutaneous pancreatic mouse model study schedule. (B) Cell viability of Panc02 cells incubated with different concentrations of samples with or without laser irradiation. (C) Representative fluorescence images of live/dead dual-stained Panc02 cells after treatment with PBS, PBS + laser, cRGD-CPNPs, or cRGD-CPNPs + laser. (D) Tumor temperature changes of tumor-bearing mice treated with PBS, cRGD-CPNPs, PBS + laser, CPNPs + laser irradiation, and cRGD-CPNPs + laser irradiation, respectively, were monitored using a thermal imager. (E and F) Changes in the relative tumor volumes (E) and individual tumor volumes (F) seen for tumor-bearing mice in the PBS, cRGD-CPNPs, PBS + laser, CPNPs + laser, and cRGD-CPNPs + laser groups. *p <0.05. (G) Photos of tumors excised from the study mice at the end treatment (i.e., 18 days post-initial injection). (H) HE tumor-stained images of the different groups. (I) Body weight changes seen for the different tumor-bearing mice groups. (J) Legend for the curves for Figures 5D-5I. Laser irradiation: 1064 nm, 5 min, 1 W/cm^2.

To provide further support for the above suggestion, in vivo PA guided PTT studies were carried out using an orthotopic pancreatic tumor mouse model. The treatment schedule is shown in Figure 6A. Briefly, tumor-bearing BALB/c nude mice were randomly divided into five groups (n = 5/group): G1, PBS; G2, cRGD-CPNPs; G3, PBS + laser; G4, CPNPs + laser; G5, cRGD-CPNPs + laser. An NIR-II laser fiber needle was inserted into the abdominal cavity of the mouse under study and for the light groups used to photoirradiate the pancreatic tumor *in situ* (5 min, 1064 nm, 1 W/cm^2). As can be seen from inspection of the infrared thermal images shown in Figure 6B and C, a rapid rise in temperature was observed in the cRGD-CPNPs + laser group (53.6^{o}C). In contrast, the corresponding temperature increases in the PBS + laser and CPNPs + laser groups were 41.5 ^{o}C and 46.2 ^{o}C, respectively (Figure 6B and C). Bioluminescence imaging (BLI) was used to monitor the growth of the tumor (Figure 6D and E). Compared to the other groups, the lowest BLI signal in the tumor area (red circles) was seen in the cRGD-CPNPs + laser group. After treatment, a lot of BLI signal was seen in the abdominal region (yellow circles) in the control groups, likely due to the presence of intra-abdominal tumor metastases.[54-55] On the other hand, the abdominal BLI signal in the cRGD-CPNPs + laser group was relatively low. This finding leads us to suggest that PTT combined with cRGD-CPNPs could inhibit the generation of intra-abdominal metastases, as inferred from this orthotopic pancreatic tumor model (Figure 6D, E and Figure S14). At the end of treatment, the pancreatic tissues from different groups were excised; again, the lowest BLI signal was seen in the cRGD-CPNPs + laser group compared to the other groups (Figure 6F and G). Hematoxylin and eosin (HE) staining studies provided further support for the proposed efficacy

of the putative cRGD-CPNPs + laser treatment (Figure 6H).

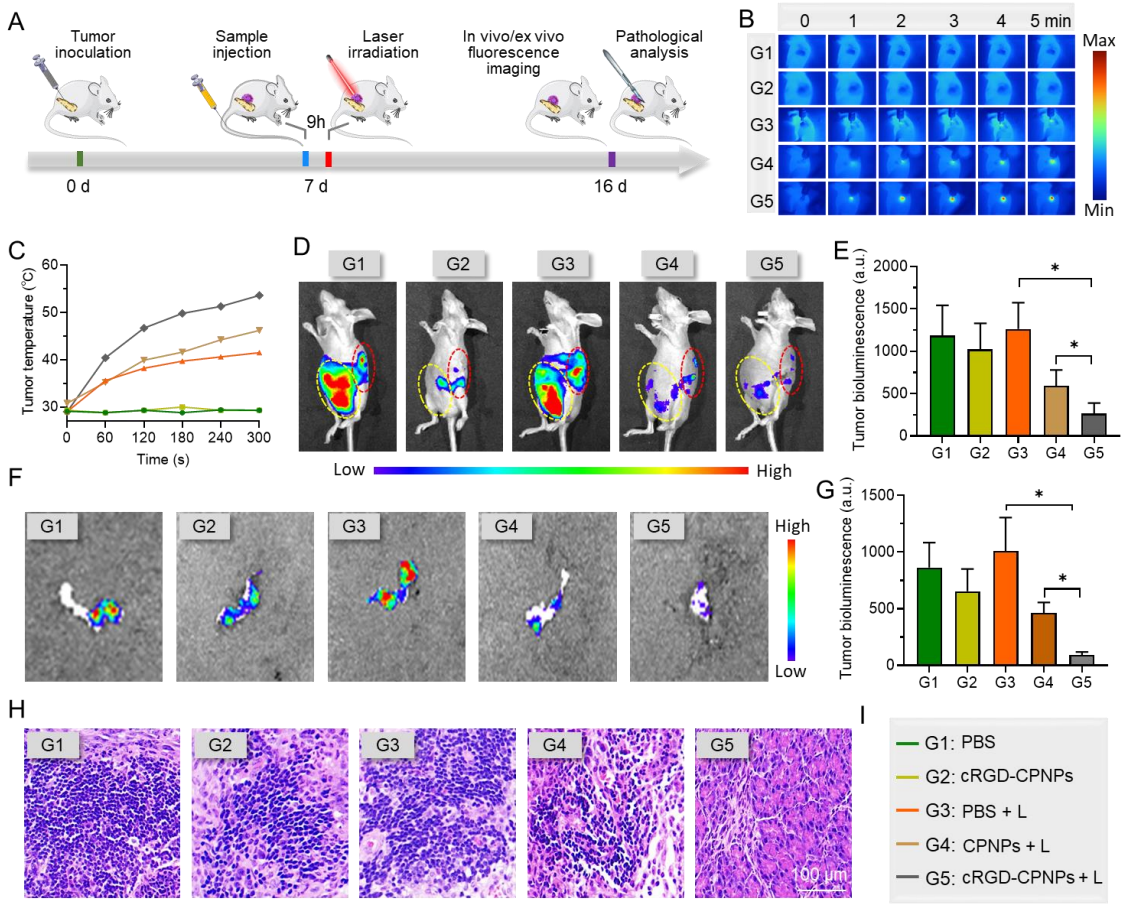

Figure 6. In vivo PA guided PTT in an orthotopic pancreatic tumor model. (A) In vivo PTT of orthotopic pancreatic mouse model and associated study schedule. (B and C) Infrared thermal images and temperature changes of tumor in the tumor-bearing mice. (D and E) Bioluminescence images and corresponding quantitative results for tumor-bearing mice at the end of treatment corresponding to different groups. Red dotted circles indicate orthotopic pancreatic regions; yellow dotted circles indicate tumor intra-abdominal metastases. *p <0.05. (F and G) Bioluminescence images and quantitative results of pancreatic tissue excised at the end of treatment for different groups. *p <0.05. (H) HE staining images of tumor tissues in different groups. Scale bar =100 μm. (I) Legend for the curves in Figures 6B-6G. Laser irradiation: 1064 nm, 5 min, 1 W/cm^2.

Biosafety Evaluation. Further biosafety assessments of the cRGD-CPNPs were carried out in vitro and in vivo in the absence of laser irradiation. Hemolytic (damage to red blood cells) analyses revealed good hemocompatibility for red blood cells treated with cRGD-CPNPs (≤15% hemolysis; Figure S15). When Panc02 cells were treated with cRGD-CPNPs at a concentration of up to 0.1 mg/mL, ≥85% viability was seen after 24 h (Figure S16). PAI was also used to monitor in real time the liver and kidneys of mice before and after injection of cRGD-CPNPs (Movies S1 and S2). As shown in Figure 7A, enhanced PA signals were seen in both organs whose intensity peaked at 9 h and 1 h, respectively, before decreasing to near pre-injection levels within 24 h (Figure 7B). The PA signal in the liver was much higher than in the kidney. These findings are consistent with the cRGD-CPNPs being cleared primarily through the liver over the course of about one day. Further support for these PA results came from biodistribution and pharmacokinetics studies (cf. Figure S17). Hematological and histological analyses were carried out on healthy mice treated with cRGD-CPNPs over a period of 7 days. No statistically significant differences between the cRGD-CPNPs treated mice and those treated with PBS were seen (Figure 7C). Likewise, no apparent differences in several key renal function indicators, including alanine aminotransferase (ALT), aspartate aminotransferase (AST), blood urea nitrogen (BUN), and creatinine (Cr), were seen for the cRGD-CPNPs and PBS treated groups (Figure 7D). Lastly, HE staining revealed no obvious tissue damage or inflammatory lesions in the liver and kidneys (Figure 7E) or other major organs (e.g., heart, spleen, and lung; Figure S18). On this basis, we suggest that the cRGD-CPNPs possess a biosafety profile adequate for use as PAI-guided PTT agents.

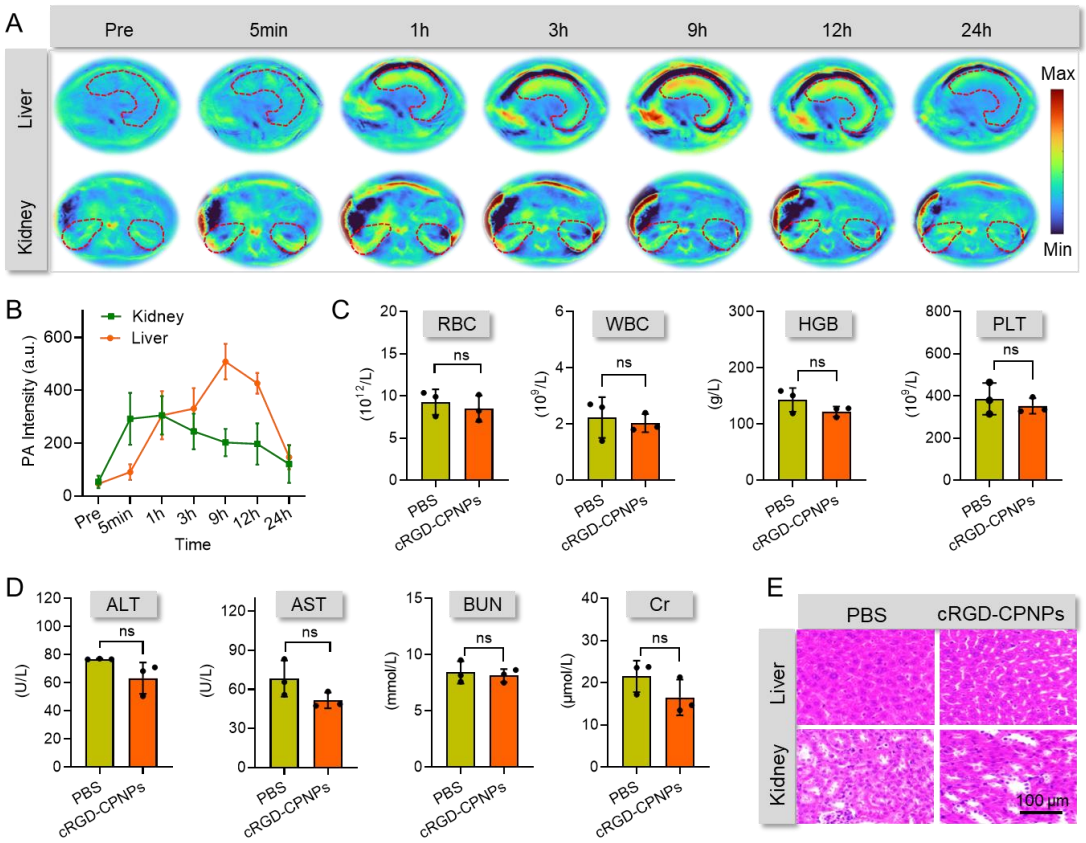

Figure 7. Biosafety evaluation by PA tomography in vivo. (A) PA signals of the liver and kidney in mice before and after intravenous injection of cRGD-CPNPs (in PBS, 150 μL, 15 mg/kg). (B) PA intensities of liver and kidney of mice before and after injection of cRGD-CPNPs. (C) Number of red blood cells (RBC), white blood cells (WBC), hemoglobin concentration (HGB), and platelet levels (PLT) of healthy BALB/c nude mice at 7 days post intravenous injection of PBS and cRGD-CPNPs, respectively. (D) Blood test of liver and renal function of healthy BALB/c nude mice at 7 days post intravenous injection of PBS and cRGD-CPNPs, respectively. ALT: alanine aminotransferase; AST: aspartate aminotransferase; BUN: blood urea nitrogen; CR: creatinine. ns, not statistically significant compared to PBS (control) group (p >0.05). (E) Representative HE stained images of the liver and kidney of a mouse treated with cRGD-CPNPs (15 mg/kg) through intravenous injection after 7 d. Scale bar = 100 μm.

CONCLUSION

In summary, we have developed a set of water soluble NIR-II absorbing nanoparticles, cRGD-CPNPs. These NPs comprise an expanded porphyrin, cyclo[8]pyrrole, encapsulated within DSPE-PEG_{2000} bearing an cRGD tumor targeting moiety. A non-targeting control system CPNPs was also prepared. The cRGD-CPNPs were shown to target pancreatic cancer with a maximum accumulation being observed 9 h post-injection using a ring-array PA tomography system. Differentiation between tumors and paracological tissues was seen in both subcutaneous and orthotopic pancreatic cancer models, as confirmed by histological analyses. In combination with NIR-II photoirradiation, the cRGD-CPNPs demonstrated greater antitumor efficacy relative to various controls, including CPNPs + Laser. These favorable results are ascribed to the enhanced tumor targeting imparted by the cRGD moiety in the cRGD-CPNPs. In the absence of laser, the cRGD-CPNPs displayed negligible toxicity as inferred from PA tomographic clearance studies and blood and histological analyses. We thus suggest that cRGD-CPNPs may have a role to play in photoacoustic-based imaging and photothermal-mediated treatment of pancreatic cancer.

ASSOCIATED CONTENT

Supporting Information

The Supporting information including experimental section and Figure S1-18 can be found online.

Movie S1. PA real-time scanning of mouse before i.v. injection of cRGD-CPNPs.

Movie S2. PA real-time scanning of mouse at 9 h post i.v. injection of cRGD-CPNPs.

AUTHOR INFORMATION

Corresponding Authors

Jingqin Chen - Research Center for Biomedical Optics and Molecular Imaging, Key Laboratory of Biomedical Imaging Science and Systems, Shenzhen Institute of Advanced Technology, Chinese Academy of Sciences, Shenzhen 518055, China; orcid.org/0000-0001-5959-3988; Email: jq.chen@siat.ac.cn

Yaguang Ren - Research Center for Biomedical Optics and Molecular Imaging, Key Laboratory of Biomedical Imaging Science and Systems, Shenzhen Institute of Advanced Technology, Chinese Academy of Sciences, Shenzhen 518055, China; Email: yg.ren@siat.ac.cn

Jian Yang - Department of Hepatobiliary Surgery I, General Surgery Center, Zhujiang Hospital, Southern Medical University, Guangzhou 510280, China; Guangdong Provincial Clinical and Engineering Center of Digital Medicine, Guangzhou 510280, China; Email: yangjian486@126.com

Jonathan L. Sessler - Department of Chemistry, The University of Texas at Austin, Austin, Texas 78712-1224, USA; orcid.org/0000-0002-9576-1325; Email: sessler@cm.utexas.edu

Chengbo Liu - Research Center for Biomedical Optics and Molecular Imaging, Key Laboratory of Biomedical Imaging Science and Systems, Shenzhen Institute of Advanced Technology, Chinese Academy of Sciences, Shenzhen 518055, China; Email: cb.liu@siat.ac.cn

Authors

Rui Chen - Research Center for Biomedical Optics and Molecular Imaging, Key Laboratory of Biomedical Imaging Science and Systems, Shenzhen Institute of Advanced Technology, Chinese Academy of Sciences, Shenzhen 518055, China; Department of Hepatobiliary Surgery I, General Surgery Center, Zhujiang Hospital, Southern Medical University, Guangzhou 510280, China; Guangdong Provincial Clinical and Engineering Center of Digital Medicine, Guangzhou 510280, China; Biliary Surgical Department of West China Hospital, Sichuan University, Chengdu 610064, China

Calvin V. Chau - Department of Chemistry, The University of Texas at Austin, Austin, Texas 78712-1224, USA

Adam C. Sedgwick - Department of Chemistry, Kings College London, 7 Trinity Street, London, SE1 1DB, U.K.

Qiang Xue - Research Center for Biomedical Optics and Molecular Imaging, Key Laboratory of Biomedical Imaging Science and Systems, Shenzhen Institute of Advanced Technology, Chinese Academy of Sciences, Shenzhen 518055, China

Tao Chen - Research Center for Biomedical Optics and Molecular Imaging, Key Laboratory of Biomedical Imaging Science and Systems, Shenzhen Institute of Advanced Technology, Chinese Academy of Sciences, Shenzhen 518055, China

Silue Zeng - Research Center for Biomedical Optics and Molecular Imaging, Key Laboratory of Biomedical Imaging Science and Systems, Shenzhen Institute of Advanced Technology, Chinese Academy of Sciences, Shenzhen 518055, China; Department of Hepatobiliary Surgery I, General Surgery Center, Zhujiang Hospital, Southern Medical University, Guangzhou 510280, China

Ningbo Chen - Research Center for Biomedical Optics and Molecular Imaging, Key Laboratory of Biomedical Imaging Science and Systems, Shenzhen Institute of Advanced Technology, Chinese Academy of Sciences, Shenzhen 518055, China; The University of Hong Kong, Department of Electrical and Electronic Engineering, Hong Kong, China

Kenneth K. Y. Wong - The University of Hong Kong, Department of Electrical and Electronic Engineering, Hong Kong, China

Liang Song - Research Center for Biomedical Optics and Molecular Imaging, Key Laboratory of Biomedical Imaging Science and Systems, Shenzhen Institute of Advanced Technology, Chinese Academy of Sciences, Shenzhen 518055, China

Author Contributions

J.Q.C., R.C., C.V.C. and A.C.S. contributed equally.

Notes

The authors declare no competing financial interests.

ACKNOWLEDGMENTS

The work was supported by grants from the National Key R&D Program of China (2022YFE0132300, 2023YFF0715300, 2023YFC2411700 to C.B.L., 2020YFA0908800 to J.Q.C.); National Natural Science Foundation of China (82172008 to J.Q.C., 82122034, 82327805, 81927807 to C.B.L., 82272132 to J.Y.); Youth Innovation Promotion Association, Chinese Academy of Sciences; Shenzhen Science and Technology Innovation Grant (JCYJ20220818101403008 to C.B.L.); Key Laboratory of Biomedical Imaging Science and System, Chinese Academy of Sciences; CAS Key Laboratory of Health Informatics (2011DP173015 to C.B.L.); Guangdong Provincial Key Laboratory of Biomedical Optical Imaging (2020B121201010 to J.Q.C.); Shenzhen Key Laboratory for Molecular Imaging (ZDSY20130401165820357 to L.S.); Basic and Applied Basic Research Foundation of Guangdong Province (2019A1515110727 to Y.G.R); The work in Austin was supported by the Robert A. Welch Foundation (F-0018 to J.L.S.) and by NIH grant RO1 CA68682 subsequent to June of 2022.

REFERENCES

1. Mizrahi, J. D.; Surana, R.; Valle, J. W.; Shroff, R. T., Pancreatic cancer. *The Lancet* **2020,** *395* (10242), 2008-2020.
2. Rawla, P.; Sunkara, T.; Gaduputi, V., Epidemiology of pancreatic cancer: global trends, etiology and risk factors. *World J. Oncol.* **2019,** *10* (1), 10.
3. Lan, L.; Evan, T.; Li, H.; Hussain, A.; Ruiz, E. J.; Zaw Thin, M.; Ferreira, R. M. M.; Ps, H.; Riising, E. M.; Zen, Y.; Almagro, J.; Ng, K. W.; Soro-Barrio, P.; Nelson, J.; Koifman, G.; Carvalho, J.; Nye, E. L.; He, Y.; Zhang, C.; Sadanandam, A.; Behrens, A., GREM1 is required to maintain cellular heterogeneity in pancreatic cancer. *Nature* **2022,** *607* (7917), 163-168.
4. Enriquez, J. S.; Chu, Y.; Pudakalakatti, S.; Hsieh, K. L.; Salmon, D.; Dutta, P.; Millward, N. Z.; Lurie, E.; Millward, S.; McAllister, F., Hyperpolarized magnetic resonance and artificial intelligence: Frontiers of imaging in pancreatic cancer. *JMIR Med. Inf.* **2021,** *9* (6), e26601.
5. Louie, A. D.; Nwaiwu, C. A.; Rozenberg, J.; Banerjee, D.; Lee, G. J.; Senthoor, D.; Miner, T. J., Providing appropriate pancreatic cancer care for

people experiencing homelessness: A surgical perspective. *American Society of Clinical Oncology Educational Book* **2021,** *41*, e20-e28.
6. Lee, W.; Il An, G.; Park, H.; Sarkar, S.; Ha, Y. S.; Huynh, P. T.; Bhise, A.; Bhatt, N.; Ahn, H.; Pandya, D. N.; Kim, J. Y.; Kim, S.; Jun, E.; Kim, S. C.; Lee, K. C.; Yoo, J., Imaging Strategy that Achieves Ultrahigh Contrast by Utilizing Differential Esterase Activity in Organs: Application in Early Detection of Pancreatic Cancer. *ACS Nano* **2021,** *15* (11), 17348-17360.
7. Dimastromatteo, J.; Brentnall, T.; Kelly, K. A., Imaging in pancreatic disease. *Nat. Rev. Gastro. Hepat.* **2017,** *14* (2), 97-109.
8. Gheorghe, G.; Bungau, S.; Ilie, M.; Behl, T.; Vesa, C. M.; Brisc, C.; Bacalbasa, N.; Turi, V.; Costache, R. S.; Diaconu, C. C., Early diagnosis of pancreatic cancer: The key for survival. *Diagnostics* **2020,** *10* (11), 869.
9. Weissleder, R., Molecular imaging in cancer. *Science* **2006,** *312* (5777), 1168-71.
10. Sibille, L.; Seifert, R.; Avramovic, N.; Vehren, T.; Spottiswoode, B.; Zuehlsdorff, S.; Schäfers, M., 18F-FDG PET/CT uptake classification in lymphoma and lung cancer by using deep convolutional neural networks. *Radiology* **2020,** *294* (2), 445-452.
11. Jiang, L.; Tu, Y.; Kimura, R. H.; Habte, F.; Chen, H.; Cheng, K.; Shi, H.; Gambhir, S. S.; Cheng, Z., 64Cu-Labeled Divalent Cystine Knot Peptide for Imaging Carotid Atherosclerotic Plaques. *J. Nucl. Med.* **2015,** *56* (6), 939-44.
12. Jiang, Y.; Upputuri, P. K.; Xie, C.; Zeng, Z.; Sharma, A.; Zhen, X.; Li, J.; Huang, J.; Pramanik, M.; Pu, K., Metabolizable Semiconducting Polymer Nanoparticles for Second Near-Infrared Photoacoustic Imaging. *Adv. Mater.* **2019,** *31* (11), 1808166.
13. Nishiyama, M.; Namita, T.; Kondo, K.; Yamakawa, M.; Shiina, T., Ring-array photoacoustic tomography for imaging human finger vasculature. *J. Biomed. Opt.* **2019,** *24* (9), 096005.
14. Li, M.; Tang, Y.; Yao, J., Photoacoustic tomography of blood oxygenation: a mini review. *Photoacoustics* **2018,** *10*, 65-73.
15. Na, S.; Russin, J. J.; Lin, L.; Yuan, X.; Hu, P.; Jann, K. B.; Yan, L.; Maslov, K.; Shi, J.; Wang, D. J., Massively parallel functional photoacoustic computed tomography of the human brain. *Nat. Biomed. Eng.* **2022,** *6* (5), 584-592.
16. Lyu, Y.; Li, J.; Pu, K., Second Near-Infrared Absorbing Agents for Photoacoustic Imaging and Photothermal Therapy. *Small Methods* **2019,** *3* (11), 1900553.
17. Li, X.; Park, E. Y.; Kang, Y.; Kwon, N.; Yang, M.; Lee, S.; Kim, W. J.; Kim, C.; Yoon, J., Supramolecular phthalocyanine assemblies for improved photoacoustic imaging and photothermal therapy. *Angew. Chem. Int. Edit.* **2020,** *132* (22), 8708-8712.
18. Zheng, Z.; Jia, Z.; Qin, Y.; Dai, R.; Chen, X.; Ma, Y.; Xie, X.; Zhang, R., All-in-One Zeolite–Carbon-Based Nanotheranostics with Adjustable NIR-II Window Photoacoustic/Fluorescence Imaging Performance for Precise NIR-II Photothermal-Synergized Catalytic Antitumor Therapy. *Small* **2021,** *17* (41), 2103252.
19. Chen, J.; Zeng, S.; Xue, Q.; Hong, Y.; Liu, L.; Song, L.; Fang, C.; Zhang, H.; Wang, B.; Sedgwick, A. C.; Zhang, P.; Sessler, J. L.; Liu, C.; Chen, J., Photoacoustic image-guided biomimetic nanoparticles targeting rheumatoid arthritis. *Proc. Natl. Acad. Sci. U. S. A* **2022,** *119* (43), e2213373119.
20. Jiang, Y.; Li, J.; Zhen, X.; Xie, C.; Pu, K., Dual-Peak Absorbing Semiconducting Copolymer Nanoparticles for First and Second Near-Infrared Window Photothermal Therapy: A Comparative Study. *Adv. Mater.* **2018,** *30* (14), 1705980.
21. Huynh, E.; Lovell, J. F.; Helfield, B. L.; Jeon, M.; Kim, C.; Goertz, D. E.; Wilson, B. C.; Zheng, G., Porphyrin shell microbubbles with intrinsic ultrasound and photoacoustic properties. *J. Am. Chem. Soc.* **2012,** *134* (40), 16464-16467.
22. Lovell, J. F.; Jin, C. S.; Huynh, E.; Jin, H.; Kim, C.; Rubinstein, J. L.; Chan, W. C.; Cao, W.; Wang, L. V.; Zheng, G., Porphysome nanovesicles generated by porphyrin bilayers for use as multimodal biophotonic contrast agents. *Nat. Mater.* **2011,** *10* (4), 324-332.
23. Ren, Y.; Sedgwick, A. C.; Chen, J.; Thiabaud, G.; Chau, C. V.; An, J.; Arambula, J. F.; He, X.-P.; Kim, J. S.; Sessler, J. L., Manganese (II) texaphyrin: A paramagnetic photoacoustic contrast agent activated by near-IR light. *J. Am. Chem. Soc.* **2020,** *142* (38), 16156-16160.
24. Jin, G.-Q.; Chau, C. V.; Arambula, J. F.; Gao, S.; Sessler, J. L.; Zhang, J.-L., Lanthanide porphyrinoids as molecular theranostics. *Chem. Soc. Rev.* **2022**, *51*, 6177-6209
25. Xu, C.; Jiang, Y.; Huang, J.; Huang, J.; Pu, K., Second Near-Infrared Light-Activatable Polymeric Nanoantagonist for Photothermal Immunometabolic Cancer Therapy. *Adv. Mater.* **2021,** *33* (36), 2101410.
26. Duan, X.; Zhang, G. Q.; Ji, S.; Zhang, Y.; Li, J.; Ou, H.; Gao, Z.; Feng, G.; Ding, D., Activatable Persistent Luminescence from Porphyrin Derivatives and Supramolecular Probes with Imaging-Modality Transformable Characteristics for Improved Biological Applications. *Angew. Chem. Int. Edit.* **2022,** *61* (24), e202116174.
27. Wang, Y.; Kai, H.; Ishida, M.; Gokulnath, S.; Mori, S.; Murayama, T.; Muranaka, A.; Uchiyama, M.; Yasutake, Y.; Fukatsu, S., Synthesis of a black dye with absorption capabilities across the visible-to-near-infrared region: A Mo-mixing approach via heterometal coordination of expanded porphyrinoid. *J. Am. Chem. Soc.* **2020,** *142* (14), 6807-6813.
28. Wang, Y.; Ogasahara, K.; Tomihama, D.; Mysliborski, R.; Ishida, M.; Hong, Y.; Notsuka, Y.; Yamaoka, Y.; Murayama, T.; Muranaka, A., Near-Infrared-III-Absorbing and-Emitting Dyes: Energy-Gap Engineering of Expanded Porphyrinoids via Metallation. *Angew. Chem. Int. Edit.* **2020,** *132* (37), 16295-16300.

29. Chen, J.; Sedgwick, A. C.; Sen, S.; Ren, Y.; Sun, Q.; Chau, C.; Arambula, J. F.; Sarma, T.; Song, L.; Sessler, J. L., Expanded porphyrins: Functional photoacoustic imaging agents that operate in the NIR-II region. *Chem. Sci.* **2021,** *12* (29), 9916-9921.
30. Chen, J.; Qi, J.; Chen, C.; Chen, J.; Liu, L.; Gao, R.; Zhang, T.; Song, L.; Ding, D.; Zhang, P., Tocilizumab–Conjugated Polymer Nanoparticles for NIR-II Photoacoustic-Imaging-Guided Therapy of Rheumatoid Arthritis. *Adv. Mater.* **2020,** *32* (37), 2003399.
31. Wu, X.; Jiang, Y.; Rommelfanger, N. J.; Yang, F.; Zhou, Q.; Yin, R.; Liu, J.; Cai, S.; Ren, W.; Shin, A., Tether-free photothermal deep-brain stimulation in freely behaving mice via wide-field illumination in the near-infrared-II window. *Nat. Biomed. Eng.* **2022**, 1-17.
32. Cai, Y.; Wei, Z.; Song, C.; Tang, C.; Han, W.; Dong, X., Optical nano-agents in the second near-infrared window for biomedical applications. *Chem. Soc. Rev.* **2019,** *48* (1), 22-37.
33. Zhang, R.; Xu, H.; Yao, Y.; Ran, G.; Zhang, W.; Zhang, J.; Sessler, J. L.; Gao, S.; Zhang, J.-L., Nickel(II) Phototheranostics: A Case Study in Photoactivated H_2O_2-Enhanced Immunotherapy. *J. Am. Chem. Soc.* **2023**, *145 (42)*, 23257-23274.
34. Ge, Z.; Chen, Q.; Osada, K.; Liu, X.; Tockary, T. A.; Uchida, S.; Dirisala, A.; Ishii, T.; Nomoto, T.; Toh, K., Targeted gene delivery by polyplex micelles with crowded PEG palisade and cRGD moiety for systemic treatment of pancreatic tumors. *Biomaterials* **2014,** *35* (10), 3416-3426.
35. Alhalhooly, L.; Confeld, M. I.; Woo, S. O.; Mamnoon, B.; Jacobson, R.; Ghosh, S.; Kim, J.; Mallik, S.; Choi, Y., Single-Molecule Force Probing of RGD-Binding Integrins on Pancreatic Cancer Cells. *ACS Appl. Mater. Interfaces* **2022,** *14* (6), 7671-7679.
36. Trajkovic-Arsic, M.; Mohajerani, P.; Sarantopoulos, A.; Kalideris, E.; Steiger, K.; Esposito, I.; Ma, X.; Themelis, G.; Burton, N.; Michalski, C. W., Multimodal molecular imaging of integrin αvβ3 for in vivo detection of pancreatic cancer. *J. Nucl. Med.* **2014,** *55* (3), 446-451.
37. Guo, B.; Chen, J.; Chen, N.; Middha, E.; Xu, S.; Pan, Y.; Wu, M.; Li, K.; Liu, C.; Liu, B., High-Resolution 3D NIR-II Photoacoustic Imaging of Cerebral and Tumor Vasculatures Using Conjugated Polymer Nanoparticles as Contrast Agent. *Adv. Mater.* **2019,** *31* (25), e1808355.
38. Yang, Y.; Chen, J.; Yang, Y.; Xie, Z.; Song, L.; Zhang, P.; Liu, C.; Liu, J., A 1064 nm excitable semiconducting polymer nanoparticle for photoacoustic imaging of gliomas. *Nanoscale* **2019,** *11* (16), 7754-7760.
39. Wang, H.; Chang, J.; Shi, M.; Pan, W.; Li, N.; Tang, B., A dual-targeted organic photothermal agent for enhanced photothermal therapy. *Angew. Chem. Int. Edit.* **2019,** *131* (4), 1069-1073.
40. Li, J.; Wang, J.; Zhang, J.; Han, T.; Hu, X.; Lee, M. M. S.; Wang, D.; Tang, B. Z., A Facile Strategy of Boosting Photothermal Conversion Efficiency through State Transformation for Cancer Therapy. *Adv. Mater.* **2021,** *33* (51), 2105999.
41. Vong, K.; Tahara, T.; Urano, S.; Nasibullin, I.; Tsubokura, K.; Nakao, Y.; Kurbangalieva, A.; Onoe, H.; Watanabe, Y.; Tanaka, K., Disrupting tumor onset and growth via selective cell tagging (SeCT) therapy. *Sci. Adv.* **2021,** *7* (17), eabg4038.
42. Yan, H.; Chen, J.; Li, Y.; Bai, Y.; Wu, Y.; Sheng, Z.; Song, L.; Liu, C.; Zhang, H., Ultrasmall hybrid protein-copper sulfide nanoparticles for targeted photoacoustic imaging of orthotopic hepatocellular carcinoma with a high signal-to-noise ratio. *Biomater. Sci.* **2018,** *7* (1), 92-103.
43. Tang, Z.; Li, C.; Kang, B.; Gao, G.; Li, C.; Zhang, Z., GEPIA: a web server for cancer and normal gene expression profiling and interactive analyses. *Nucleic Acids Res.* **2017,** *45* (W1), W98-W102.
44. Seguin, L.; Kato, S.; Franovic, A.; Camargo, M. F.; Lesperance, J.; Elliott, K. C.; Yebra, M.; Mielgo, A.; Lowy, A. M.; Husain, H., An integrin β3–KRAS–RalB complex drives tumour stemness and resistance to EGFR inhibition. *Nat. Cell Biol.* **2014,** *16* (5), 457-468.
45. Gajbhiye, K.; Gajbhiye, V.; Siddiqui, I. A.; Gajbhiye, J., cRGD functionalised nanocarriers for targeted delivery of bioactives. *J. Drug Target.* **2019,** *27* (2), 111-124.
46. Nan, P.; Dong, X.; Bai, X.; Lu, H.; Liu, F.; Sun, Y.; Zhao, X, Tumor-stroma TGF-β1-THBS2 feedback circuit drives pancreatic ductal adenocarcinoma progression via integrin αvβ3/CD36-mediated activation of the MAPK pathway. *Cancer Lett.* **2022**, *528*, 59-75.
47. Chen, T.; Liu, L.; Ma, X.; Zhang, Y.; Liu, H.; Zheng, R.; Ren, J.; Zhou, H.; Ren, Y.; Gao, R.; Chen, N.; Zheng, H.; Song, L.; Liu, C., Dedicated Photoacoustic Imaging Instrument for Human Periphery Blood Vessels: A New Paradigm for Understanding the Vascular Health. *IEEE. Trans. Biomed. Eng.* **2022,** *69* (3), 1093-1100.
48. Zhang, Y.; Wang, L., Video-rate ring-array ultrasound and photoacoustic tomography. *IEEE Trans. Med. Imaging* **2020,** *39* (12), 4369-4375.
49. Jeng, G.-S.; Li, M.-L.; Kim, M.; Yoon, S. J.; Pitre, J. J.; Li, D. S.; Pelivanov, I.; O'Donnell, M., Real-time interleaved spectroscopic photoacoustic and ultrasound (PAUS) scanning with simultaneous fluence compensation and motion correction. *Nat. Commun.* **2021,** *12* (1), 1-12.
50. Li, W.; Little, N.; Park, J.; Foster, C. A.; Chen, J.; Lu, J., Tumor-associated fibroblast-targeting nanoparticles for enhancing solid tumor therapy: progress and challenges. *Mol. Pharm.* **2021,** *18* (8), 2889-2905.
51. Dewhirst, M. W.; Secomb, T. W., Transport of drugs from blood vessels to tumour tissue. *Nat. Rev. Cancer* **2017,** *17* (12), 738-750.
52. MacCuaig, W. M.; Fouts, B. L.; McNally, M. W.; Grizzle, W. E.; Chuong, P.; Samykutty, A.; Mukherjee, P.; Li, M.; Jasinski, J. B.; Behkam, B.;

McNally, L. R., Active Targeting Significantly Outperforms Nanoparticle Size in Facilitating Tumor-Specific Uptake in Orthotopic Pancreatic Cancer. *ACS Appl. Mater. Interfaces* **2021,** *13* (42), 49614-49630.

53. Zhao, L.; Liu, Y.; Xing, R.; Yan, X., Supramolecular photothermal effects: a promising mechanism for efficient thermal conversion. *Angew. Chem. Int. Edit.* **2020,** *132* (10), 3821-3829.
54. Li, S.; Shang, L.; Xu, B.; Wang, S.; Gu, K.; Wu, Q.; Sun, Y.; Zhang, Q.; Yang, H.; Zhang, F.; Gu, L.; Zhang, T.; Liu, H., A Nanozyme with Photo-Enhanced Dual Enzyme-Like Activities for Deep Pancreatic Cancer Therapy. *Angew. Chem. Int. Edit.* **2019,** *58* (36), 12624-12631.
55. Zhu, Z.; Wang, Q.; Chen, X.; Wang, Q.; Yan, C.; Zhao, X.; Zhao, W.; Zhu, W. H., An Enzyme-Activatable Aggregation-Induced-Emission Probe: Intraoperative Pathological Fluorescent Diagnosis of Pancreatic Cancer via Specific Cathepsin E. *Adv. Mater.* **2022,** *34* (3), e2107444.

TOC graphic


Excited state
H_2SO_4
NIR-II
Excitation
Fluorescence
Nonradiative decay
PAI
PTT
Cyclo[8]pyrrole
Ground state